FLUIDIC THRUST VECTORING OF LOW OBSERVABLE AIRCRAFT

Mark S. Mason, William J. Crowther
University of Manchester, School of Engineering, Oxford Road, Manchester M15 9PL

Abstract

The work presented in this paper deals with the development of a coflow fluidic thrust vectoring system for use on a low observable unmanned air vehicle operating in the subsonic flight regime.

Two approximately 1/10th scale fluidic thrust vectoring demonstrator rigs were designed and built in order to investigate the effect of various geometric variables on thrust vectoring effectiveness. These included secondary gap height, *dh*, and Coanda surface diameter, *Æ*. Load measurements were obtained using a six component overhead balance. The thrust vector force, $F_{z,tv}$, was made non-dimensional using the thrust force of the non-vectored primary jet, F_x, to give a thrust vector coefficient, C_z. Tests were carried out over the mass flow ratio range $0 \quad m_s/m_p < 0.13$ which corresponded to a momentum flow ratio range of $0 \quad M_s/M_p < 0.4$. A computational investigation for 2D flow was also undertaken primarily to aid in the design of the experimental demonstrator rigs and smoke flow visualisation techniques were used to further investigate the flow characteristics of a non-vectored and a vectored primary jet.

The investigation shows that both the experimental and computational results obtained follow a similar trend line. A 'dead zone' appears at low mass flow ratios in which no control can be achieved. There then follows a control region in which continuous thrust vector control can be achieved followed by a hypothetical saturation region. The secondary jet blowing rate, the Coanda surface diameter and the primary nozzle to secondary nozzle height ratio are seen to determine whether effective and efficient fluidic thrust vectoring can be achieved.

Nomenclature

A_p	Cross sectional area of primary jet	m^2
A_s	Cross sectional area of secondary jet	m^2
AR	Jet aspect ratio	
C_z	Thrust vector coefficient	
$C_{z,max}$	Maximum thrust vector coefficient	
dh	Secondary gap height	m
F_x	Thrust	N
$F_{z,tv}$	Thrust vector force	N
h	Primary jet height	m
L	Primary jet length	m
m_p	Primary mass flow ($=\rho A_p V_p$)	kg/s
M_p	Primary momentum flow ($=\rho A_p V_p^2$)	kgm/s^2
m_s	Secondary mass flow ($=\rho A_s V_s$)	kg/s
M_s	Secondary momentum flow ($=\rho A_s V_s^2$)	kgm/s^2
$M_{z,tv}$	Thrust vector moment	Nm
P	Pressure	N/m^2
P_{atm}	Atmospheric pressure	N/m^2
V_p	Primary flow velocity	m/s
V_s	Secondary flow velocity	m/s
V	Freestream velocity	m/s
T_o	Resultant thrust	N
d_{tv}	Thrust vector angle	o
ρ	Air density	kg/m^3
Æ	Coanda surface diameter	m

Abbreviations

CFD	Computational fluid dynamics
MATV	Multi-axis thrust vectoring
TV	Thrust vectoring
UAV	Unmanned air vehicle

1 Introduction

Thrust vectoring of aircraft is emerging as a key technology for current and future air vehicles. The primary challenge is to develop a multi axis thrust vectored exhaust nozzle which can operate effectively at all flight conditions whilst satisfying the design constraints of low cost, low weight and minimal impact on radar cross section signature. A current state of the art two axis mechanical thrust vectoring system will be incorporated into the Lockheed/Martin F-22 Raptor project [1].

Thrust vectoring is a manoeuvre effector which can be used to augment aerodynamic control moments throughout and beyond the conventional flight envelope. Using thrust vectoring at high angles of attack where conventional control surfaces become redundant can lead to the concept of a supermanoeuvrable air vehicle able to maintain control at angles of attack greater than 90 degrees. Thrust vector control at low angles of attack enables the reduction in size of horizontal and vertical tails and a consequent reduction in aircraft drag.

There are two methods of achieving thrust vectoring - either mechanically or by fluidic control. Mechanical thrust vectoring involves deflecting the engine nozzle and thus physically changing the direction of the primary jet [2]. Fluidic thrust vectoring involves injecting fluid into or removing it from the boundary layer of a primary jet to enable vectoring. Although a mechanical thrust vectoring system is effective, it can be heavy, complex, difficult to integrate and aerodynamically inefficient [3]. A fluidic thrust vectoring system has the advantage of being lightweight, simple, inexpensive and free from moving parts (fixed geometry), and can be potentially implemented with minimal aircraft observability penalty.

A fluidic thrust vectoring system must, however, be implemented at the outset of the design process unlike a mechanical system which can be retrofitted to existing aircraft currently in use today (see NASA F-15 ACTIVE flight programme [4]).

Various types of fluidic thrust vectoring techniques have been discussed in the literature namely shock thrust vector, coflow and counterflow control (figure 1).

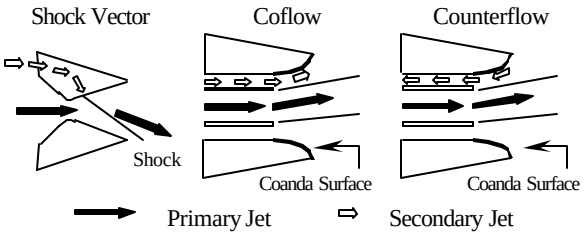

Figure 1 *Types of fluidic thrust vector control concepts*

Shock thrust vector control involves injecting a secondary jet into the primary jet from one of the divergent flaps. An oblique shock wave is formed which deflects the primary jet in the pitch plane [5]. Both the counterflow and coflow concepts involve the use of a secondary jet in addition to the Coanda effect to facilitate thrust vectoring. The former technique uses momentum removal whereas the latter uses momentum injection to control the primary jet. In their studies, Van der Veer and Strykowski [6] investigated the counterflow technique in which Coanda surfaces are positioned at the exit of the primary jet and a vacuum is applied to a slot adjacent to it. Experiments were carried out for various nozzle geometries and it was found that whilst a high thrust vector force, $F_{z,tv}$, was achieved at relatively low secondary jet blowing rates, the technique caused the primary jet to attach itself to the Coanda surface.

In the present work, a coflow fluidic thrust vectoring system is being developed for use on low observable unmanned air vehicles operating in the subsonic flight regime. In this study, a 2D, pitch only, fluidic thrust vectoring demonstrator has been developed to investigate vectoring effectiveness for various jet geometries with zero freestream velocity (V = 0). The effects of increasing secondary jet blowing rates, Coanda surface geometry and secondary jet gap height on the forces generated have been measured using a six component overhead balance. Smoke flow visualisation and a computational investigation assuming 2D flow have also been undertaken to augment the physical understanding of the experimental results obtained.

2 Coflow Fluidic Thrust Vectoring

Coflow thrust vectoring is achieved by utilising the Coanda effect [7] to alter the angle of the primary jet from an engine exhaust nozzle. The Coanda effect is the tendency of a moving fluid to adhere to a solid curved surface. Due to the presence of the Coanda surface, entrainment by the secondary jet is inhibited on the side nearest to the surface (figure 2).

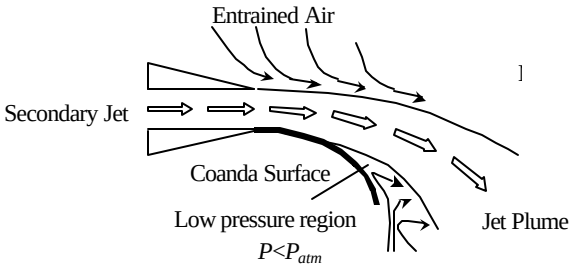

Figure 2 *The Coanda effect (incident jet tends to remain attached to a convexly curved surface)*

This entrained air must then accelerate over the Coanda surface producing a local low-pressure region, which results in a pressure gradient perpendicular to the primary jet centreline. The increased entrainment rate on the side of the secondary jet unbounded by the Coanda surface coupled with the receptivity of the primary jet fluid to small changes in the local flow field facilitates thrust vectoring. By positioning curved surfaces to the rear of the engine nozzle of an aircraft and introducing a secondary stream of coflowing air parallel to the Coanda surface, thrust vectoring of an aircraft can be achieved (figure 3).

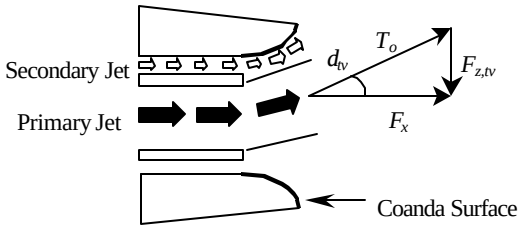

Figure 3 *Coflow thrust vectoring concept used in the present work (aircraft coordinate system)*

The resultant thrust vector normal force generated on the Coanda surface, $F_{z,tv}$, produces a pitching moment, $M_{z,tv}$, about the aircraft's centre of gravity thus enabling the aircraft to be trimmed during flight. In the present work, this force has been made non-dimensional to give a thrust vector coefficient, C_z:

$$C_z = \frac{F_{z,tv}}{T_o} \tag{1}$$

C_z is related to the thrust vector angle as follows:

$$\delta_{tv} = \tan^{-1} C_z \tag{2}$$

Note that thrust vectoring incurs a drag penalty. When $d_{tv} > 0$, the actual thrust of the primary jet will be lower than the resultant thrust i.e. $F_x < T_o$.

3 Demonstrator Models

An approximately $1/10^{th}$ scale rig with a rectangular nozzle was designed in order to demonstrate fluidic thrust vectoring in the low subsonic flight regime. The aspect ratio, *AR*, of the nozzle was 4.7 (figure 4).

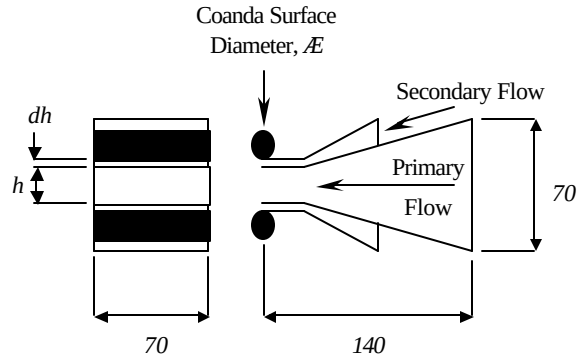

Figure 4 *Schematic of fluidic thrust vectoring rig (Dimensions in mm)*

Two demonstrator jet rigs were constructed (figure 5) in order to investigate the effect of the gap height, *dh*, of the secondary jet (rig a) and Coanda surface diameter, *Æ*, (rig b) on fluidic thrust vectoring effectiveness. In the present work the secondary jet slot height and Coanda surface diameter were made non-dimensional using the primary jet height, *h*.

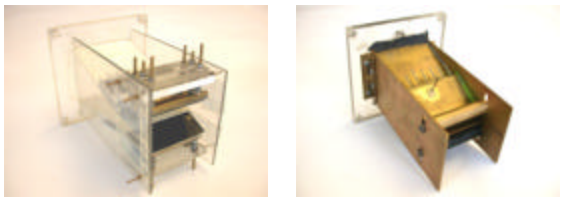

(a) Varying gap height (dh/h) *(b) Varying surface diameter (Æ/h)*

Figure 5 *Fluidic thrust vectoring demonstrator rigs*

4 Experimental Procedure

A series of experimental tests were carried out in order to determine the thrust vector coefficients, C_z, of the jet rigs. These range of tests were conducted at increasing secondary mass flow rates, m_s, up to approximately 13% of the primary flow rate, m_p, which corresponded to secondary momentum flow rates, M_s, up to approximately 40% of the primary momentum flow rate, M_p. This range of secondary flow rates made it possible to obtain an overall picture of the flow characteristics of the vectored jet. Jet configurations in the range 0 *dh/h* 0.08 and 0 *Æ/h* 1 were used as test cases.

4.1 Force Data Load measurements were obtained using a six component overhead balance. The demonstrator jet rig was attached to a centrifugal fan unit to provide the primary jet flow velocity, V_p » 19 (m_p » 0.024, M_p » 0.46). Compressed air available in the laboratory supplied the secondary airflow. The secondary mass flow rates were controlled using a pressure regulator with flow rates measured using a vertical rotameter. Thrust force, F_x, and thrust vector force, $F_{z,tv}$, measurements were obtained at increasing secondary jet blowing rates for the following demonstrator configurations (table 1):

Const. Æ/h	*dh/h*	*Const. dh/h*	*Æ/h*
3.3 ⟷	0.013	0.04 ⟷	0
3.3 ⟷	0.026	0.04 ⟷	0.33
3.3 ⟷	0.040	0.04 ⟷	0.50
3.3 ⟷	0.053	0.04 ⟷	0.66
3.3 ⟷	0.066	0.04 ⟷	0.83
3.3 ⟷	0.080	0.04 ⟷	1

Table 1 *Experimental configurations used in this study*

4.2 CFD Simulation A computational investigation for 2D flow was undertaken primarily to aid in the design of the experimental demonstrator rigs. The standard k-ε turbulence model was used to simulate the nozzle flows in this study. The computational domain was created using an unstructured meshing scheme consisting of triangular elements (No. of cells = 43,237). The effects of Coanda surface geometry and secondary gap height on vectoring effectiveness for increasing secondary jet blowing rates were investigated. The CFD simulations provided force data which were then compared to the experimental data obtained.

4.3 Smoke Flow Visualisation Smoke was injected into the intake of the centrifugal fan unit. The resulting plume was illuminated using two high powered (1000W) spotlights and images were captured using a digital video camera at a shutter speed of 1/10,000s. Smoke flow visualisation was carried out on a demonstrator jet rig with *dh/h* = 0.04 and *Æ/h* = 1 for 0 m_s/m_p < 0.13.

5 Experimental Results and Discussion

A systematic series of static tests were carried out in order to determine the characteristics of the primary jet in its vectored state.

5.1 Varying Secondary Gap Height (*dh/h*) Figure 6 shows the relationship between the mass flow ratio and the resulting thrust vector coefficient for various secondary gap heights at a constant Coanda surface diameter of *Æ/h* = 3.3. Six secondary gap heights were tested in the range 0 *dh/h* 0.08. The results show that as the secondary jet blowing rate is increased, the thrust vector coefficient increases. It can be seen that as the secondary gap height increases, the values obtained for C_z decrease accordingly at each mass flow ratio tested. All of

the following results are based on the aircraft coordinate system.

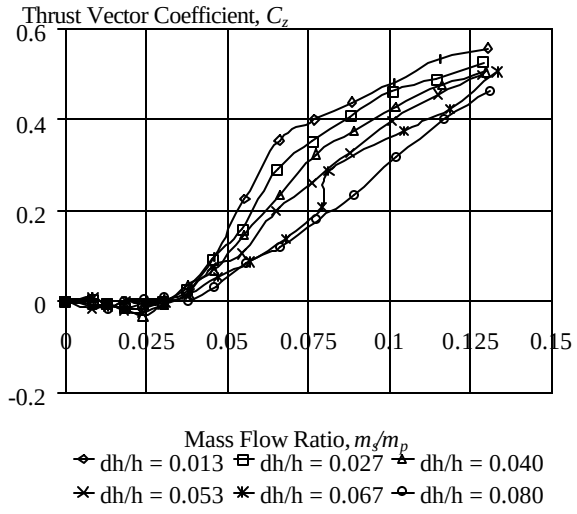

Figure 6 *Thrust vector coefficient values at increasing secondary jet blowing rates for various secondary gap heights at constant Coanda surface diameter Æ/h = 3.3.*

5.2 Varying Coanda Surface Diameter (*Æ/h*) Figure 7(a and b) shows the relationship between the mass flow ratio, the momentum flow ratio and the resulting thrust vector coefficient for various Coanda surface diameters at a constant secondary gap height ratio of *dh/h* = 0.04. Six Coanda surface diameters were tested in the range 0 *Æ/h* 1. A value of 0 indicates that no Coanda surfaces were present. As shown in figure 7(a and b), an increase in secondary jet blowing rate results in an increase in the value of C_z, and as the Coanda surface diameter is increased the gradient of the curve becomes steeper once the 'dead zone' has been overcome.

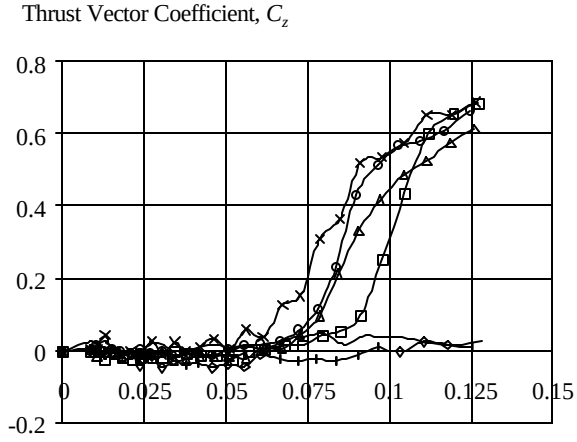

(a) Mass Flow Ratio, m_s/m_p

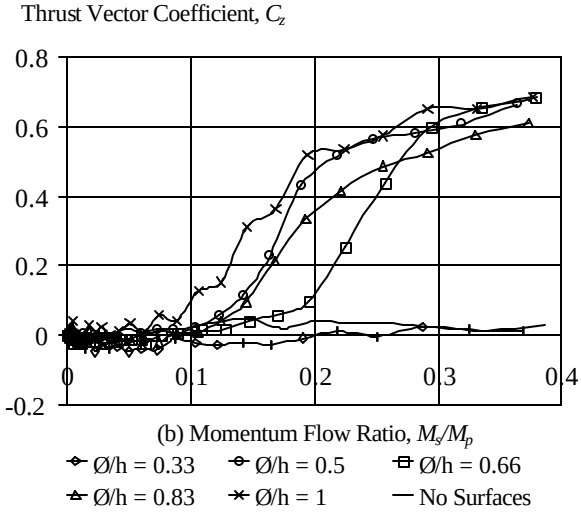

Figure 7 *Thrust vector coefficient at increasing secondary jet blowing rates for (a) m_s/m_p and (b) M_s/M_p for various Coanda surface diameters at constant dh/h = 0.04*

The diameter of the Coanda surface also determines the size of the 'dead zone' and hence where the onset of the control region begins. The results show that the secondary jet is more likely to separate from a Coanda surface with a small diameter and as a consequence the 'dead zone' will be prolonged over a wider range of secondary jet blowing rate values. It is the secondary jet blowing rate, the Coanda surface diameter and the secondary jet gap height that determine whether effective and efficient fluidic thrust vectoring can be achieved

As seen in figures 6 and 7, the experimental results followed a similar trend. This is shown schematically in figure 8.

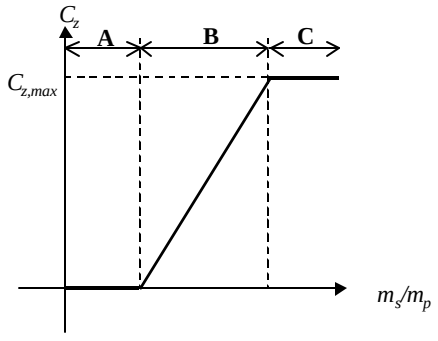

Figure 8 *Trend line of the experimental results A – Dead zone, B – Control, C – Saturation*

Figure 7(a and b) shows that at very low secondary jet blowing rates i.e. $m_s << m_p$, the thrust vector coefficient is very small and there appears to be a 'dead zone' in which no flow control can be achieved. This phenomenon can be

attributed to the fact that the Coanda effect cannot function at low secondary jet blowing rates (figure 9).

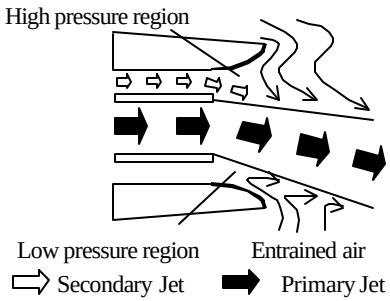

Figure 9 *Schematic of control reversal phenomenon at low secondary jet blowing rates*

At low secondary jet blowing rates, the secondary jet separates early from the Coanda surface. In extreme cases, control reversal can occur whereby the primary jet vectors in the opposite direction before vectoring in the direction expected. In this instance, the faster moving primary jet entrains the slower moving air of the secondary jet and instead of adhering to the Coanda surface and remaining attached far downstream, the secondary jet separates and a high pressure region forms. The entrainment has the effect of skewing the primary jet velocity distribution towards the opposite Coanda surface and the differential pressure gradient created vectors the primary jet in that direction. After the 'dead zone', the Coanda effect dominates and the curve enters a region in which a large increase in thrust vector coefficient can be achieved for relatively small increases in the secondary jet blowing rate. It is in this region that continuous control of the primary jet can be achieved. From here on the thrust vector coefficient, and hence the thrust vector force generated, will enter a hypothetical region of saturation i.e. the thrust vector coefficient reaches an almost constant value, $C_{z,max}$, for any increase in secondary jet blowing rate.

5.3 Computational Fluid Dynamics In each of the following cases, the jet was configured such that dh/h = 0.04, $Æ/h$ = 1 and V_p = 20.

Figure 10 shows the contours of velocity magnitude for a non-vectored primary jet (V_s = 0, m_s/m_p = 0) and figure 11 shows the contours coloured by velocity magnitude for a vectored primary jet (V_s = 35, m_s/m_p = 0.07, M_s/M_p = 0.12). In this case, the uppermost secondary jet was activated in order to vector the primary jet. It can be seen that the entrainment on the upper Coanda surface has been inhibited during vectoring. Notice the regions of recirculating flow on the Coanda surfaces.

In order to determine the feasibility of using computational fluid dynamics as a design tool in the present work, a series of tests were carried out using the above rig configuration.

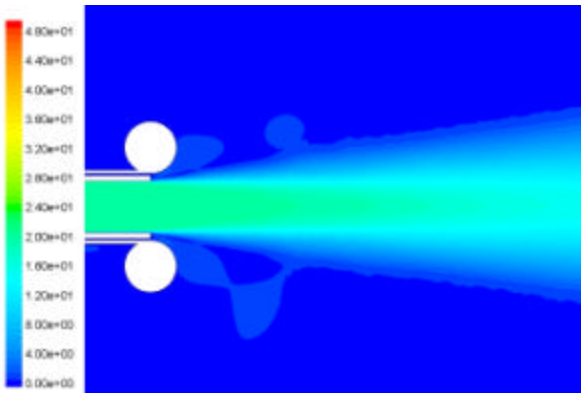

Figure 10 *Contours coloured by velocity magnitude for m_s/m_p = 0, dh/h = 0.04, $Æ/h$ = 1, C_z = 0*

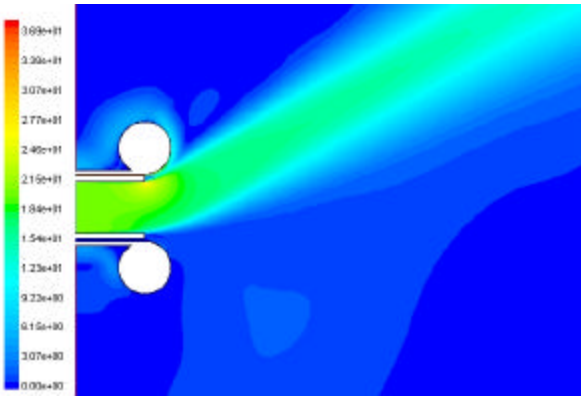

Figure 11 *Contours coloured by velocity magnitude for m_s/m_p = 0.07, dh/h = 0.04, $Æ/h$ = 1, C_z = 0.37*

The experimental results obtained were used as parameters and boundary conditions for the CFD model. A comparison between the computational and the experimental results obtained is shown in figure 12.

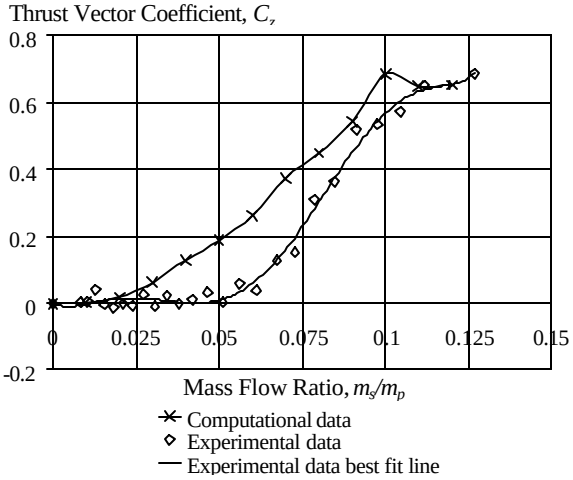

Figure 12 *Experimental and computational results showing thrust vector coefficient values for dh/h = 0.04 and $Æ/h$ = 1*

It can be seen that both curves follow a similar trend. However, the extent of the 'dead zone' for the experimental work is more prolonged than that obtained in the computational work. The computational work has also highlighted both the control and saturation regions as seen previously in the experimental results (figure 7). At low secondary jet blowing rates, the CFD investigation predicted greater thrust vector coefficients than those obtained during the experimental tests for approximately the same mass flow ratio

5.4 Smoke Flow Visualisation In each of the following cases, the jet was configured such that *dh/h* = 0.04 and *Æ/h* = 1. Figure 13 shows the visualisation of a non-vectored primary jet (V_s = 0, m_s/m_p = 0).

Figure 13 *Visualisation of a non-vectored primary jet for m_s/m_p = 0, dh/h = 0.04, Æ/h = 1, C_z = 0*

Figure 14 *Visualisation of a vectored primary jet for m_s/m_p = 0.07, dh/h = 0.04, Æ/h = 1, C_z =0.14*

Figure 14 shows a vectored primary jet (m_s/m_p =0.07, M_s/M_p = 0.12). In this case, the uppermost secondary jet was activated in order to vector the primary jet.

5.5 Experimental errors The forces generated during vectoring were only small and required a sensitive force balance reading to be made. The six-component balance used to obtain the force measurements was more sensitive in the side force plane and therefore the thrust vector force measurements were carried out in this plane. The balance continuously averaged forces over 50,000 readings and all thrust vector force point measurements were further averaged over a period of ten readings. This approach helped to minimise any errors involved during the experimental work.

6 Concluding Remarks

- Both the experimental and computational results obtained followed a similar trend line. A 'dead zone' appears at low secondary jet mass flow rates. There then follows a control region in which continuous thrust vector control can be achieved followed by a hypothetical saturation region in which the thrust vector coefficient will reach an almost constant value, $C_{z,max}$, for any increase in secondary jet blowing rate.

- The secondary jet blowing rate and the Coanda surface diameter determined whether effective and efficient fluidic thrust vectoring could be achieved. The length of the 'dead zone' was also dependent on the size of the Coanda surface diameter. A small diameter resulted in a prolonged 'dead zone' range.

- For the configurations studied above, if a thrust vector angle of 15° (C_z = 0.3) is required to trim an aircraft in flight then the minimum secondary momentum jet flow rate needed is approximately 0.07N and the thrust vector force is 0.14N. Therefore, only a gain in force of 2 has been achieved at a momentum flow ratio of 15%. This value can be improved if the ratio between the primary jet height and the secondary gap height, *dh/h*, is reduced.

Acknowledgements

The authors would like to acknowledge the help of the laboratory technicians at the Goldstein laboratory for their help and assistance throughout the course of this work. This research was funded by the EPSRC, award reference number 99315106.

References

[1] Pruden A.L. Jnr, **F-22 Air Superiority for the Start of the 21st Century,** Lockheed Horizons, pp 30-36, August 1992.

[2] Gal-Or B., **Fundamental Concepts of Vectored Propulsion,** Journal of Propulsion v 6 No.6, Nov-Dec 1990.

[3] Hunter C.A. and Deere K.A., **Computational Investigation of Fluidic Counterflow Thrust Vectoring,** AIAA Paper No. 99-2669, June 1999.

[4] Smolka J.W. et al., **F-15 ACTIVE Flight Research Program,** Society of Experimental Test Pilots, 40th Symposium Proceedings, 1996.

[5] Wing D., **Static Investigation of Two Fluidic Thrust Vectoring Concepts on a Two Dimensional Convergent Divergent Nozzle,** NASA TM 4574, December 1994.

[6] Van der Veer M. and Strykowski P.J., **Counterflow Thrust Vector Control of Subsonic Jets: Continuous and Bistable Regimes,** Journal of Propulsion and Power v13 No.3, May-June 1997.

[7] Panitz T. and Wasan D.T., **Flow Attachment to Solid Surfaces: The Coanda Effect,** AIChE Journal v18 No.1, pp 51-57, January 1972.

Further Details

Send all correspondence to the following e-mail address:

mark.s.mason@stud.man.ac.uk

or visit the website:

http://www.geocities.com/m_mason007/home.html